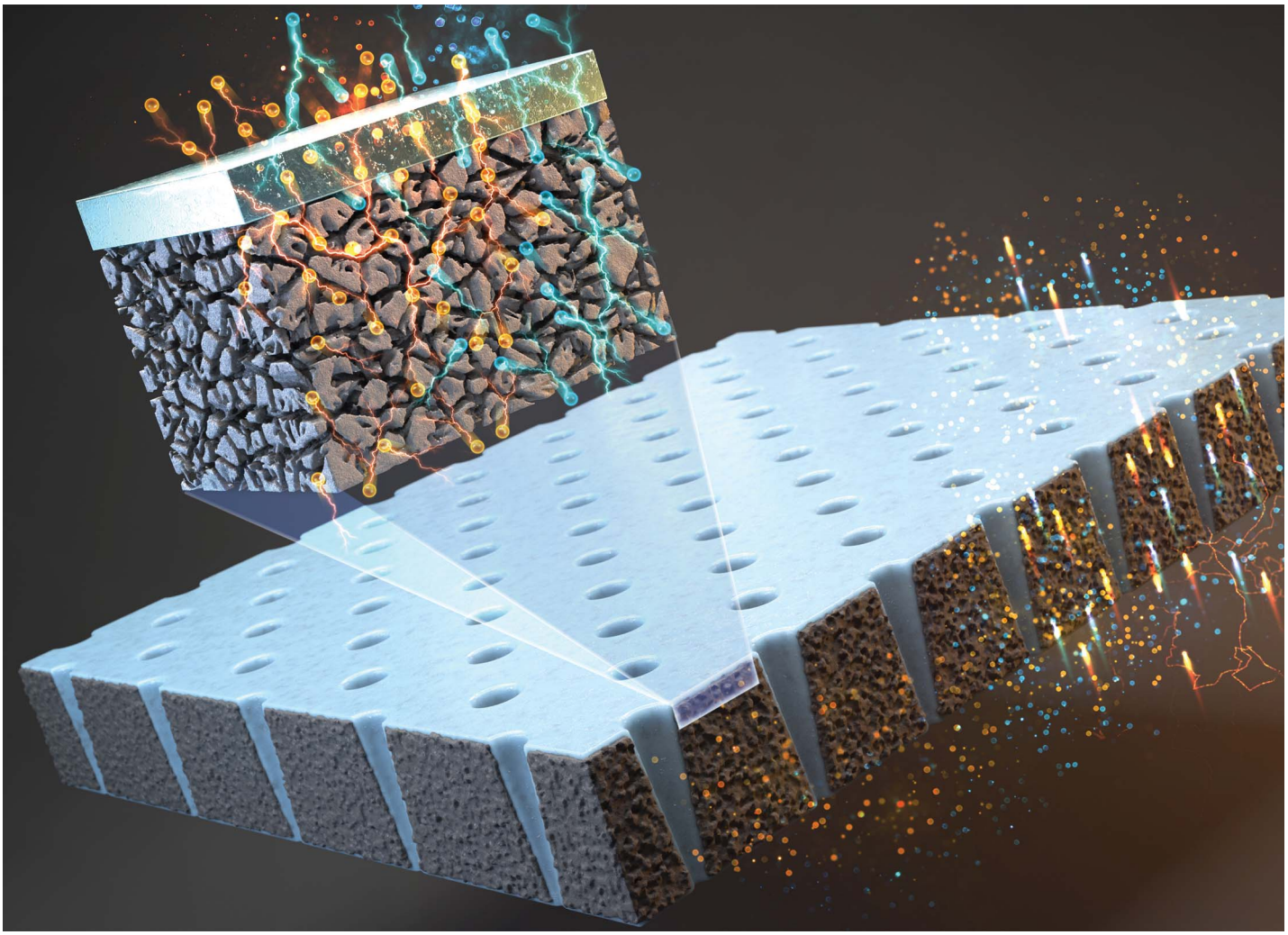

Showcasing research from Professor Tae Joo Park's laboratory, Department of Materials Science and Chemical Engineering, Hanyang University, Ansan, Republic of Korea.

Atomic-layer-deposited Ru–RuO_x mixed protective layer for improving ionic–electronic conductivity of sintered $LiCoO_2$ cathodes in Li-ion batteries

Ru–RuO_x mixed protective layers were deposited by atomic layer deposition without post-treatment, enabling improved interfacial conduction in conducting-agent-free sintered cathodes.

Image reproduced by permission of Tae Joo Park from *J. Mater. Chem. A*, 2026, **14**, 9966.

As featured in:

See Kyu Moon Kwon *et al.*, *J. Mater. Chem. A*, 2026, **14**, 9966.

ROYAL SOCIETY OF CHEMISTRY

rsc.li/materials-a

Registered charity number: 207890

Journal of Materials Chemistry A

ROYAL SOCIETY OF CHEMISTRY

PAPER

View Article Online
View Journal | View Issue

Cite this: *J. Mater. Chem. A*, 2026, **14**, 9966

Atomic-layer-deposited Ru–RuO_x mixed protective layer for improving ionic–electronic conductivity of sintered $LiCoO_2$ cathodes in Li-ion batteries

Kyu Moon Kwon, [a] Ji Won Han, [a] Joungwon Park,[b] Kyoung Hwan Kim, [b] Hwi-Yeol Park,[b] Woo-Hee Kim, [a] Ji-Hoon Ahn, [a] Hyo Rang Kang*[ac] and Tae Joo Park *[ad]

Received 3rd December 2025
Accepted 15th February 2026

DOI: 10.1039/d5ta09872f

rsc.li/materials-a

The use of high-density three-dimensional sintered (HTS) cathode plates is a promising approach for increasing the energy density of Li-ion batteries. However, their performances are limited by the absence of conducting agents and interfacial side reactions. In this study, a Ru–RuO_x mixed protective layer (RRML) is conformally deposited on HTS-$LiCoO_2$ (LCO) *via* atomic layer deposition and employed as a mixed ionic–electronic conducting protective layer. Physicochemical analyses reveal the formation of a Ru–RuO_x solid solution at a 5 nm thickness without post-treatment. The full-cell evaluation demonstrates that the RRML-coated HTS-LCO electrode exhibits approximately twice the cycle life (80% capacity retention at 1C) of uncoated HTS-LCO. This study demonstrates that the RRML coating enables simultaneous ionic and electronic conduction and interfacial stabilization.

Introduction

Li-ion batteries (LIBs) with higher energy densities and smaller form factors are increasingly required to address the growing demand for miniaturized energy-storage devices. However, the cathodes of conventional LIBs cannot achieve higher electrode densities owing to their substantial content (>5 wt%) of binders and conducting agents (CAs).[1–3] A promising approach to overcome this limitation is to eliminate both binders and CAs, while maximizing the cathode density through the sintering of the cathode active material (CAM).[4–7] For example, Kim *et al.*[7] reported the fabrication of a high-density three-dimensional sintered $LiCoO_2$ (HTS-LCO) plate that enables the removal of CAs and binders; the plate increased the CAM loading and achieved an areal capacity of 3.5 mAh cm^{-2}. However, such HTS-LCO structures exhibit extensive direct contact between the CAM surface and liquid electrolytes, which leads to undesirable side reactions. The interfacial resistance generated by these reactions, together with the CA-free architecture, amplifies polarization and accelerates capacity decay, indicating that the cathode surface requires not only chemical passivation but also a coating design that sustains charge-transport functionality under high-rate operation.[8–10]

The protective layer coating of CAMs is considered an effective strategy to address the aforementioned issues in LIBs.[11–13] Conventional wet-chemical methods, such as sol–gel and spray coating, have been widely employed but are limited in terms of thickness control and uniform surface coverage.[14] In contrast, atomic layer deposition (ALD), which relies on self-limiting surface reactions, enables conformal coating with atomic-scale thickness control, even on substrates with complex geometries. Because of this capability, ALD allows for the deposition of ultrathin films (typically a few nanometers thick) with exceptional uniformity, making it one of the most suitable techniques for protective layer formation.[15–17]

In the case of HTS-LCO, which is composed solely of an active material without any CAs, the absence of electron-percolation networks within the electrode imposes intrinsic limitations on charge-transfer kinetics, particularly under high-C-rate conditions. As a result, the protective layer is required to exhibit mixed ionic–electronic conducting (MIEC) characteristics, rather than functioning solely as a chemically inert passivation barrier.[13,18,19] Under these constraints, electronically insulating oxides (*e.g.*, Al_2O_3, TiO_2, and ZrO_2) are not suitable for CA-free sintered cathodes, where electronic percolation must be preserved. Among the platinum-group elements, Ru is known as an excellent electronic conductor owing to its short electron mean free path (≈6.6 nm) and low electrical resistivity (≈7 μΩ·cm^{-1}), even in thin films.[20,21] Moreover, RuO_x acts as an ionic conductor, exhibiting an ionic conductivity of approximately 10^{-8} S cm^{-1} and a relatively low electrical resistivity despite being an oxide.[22,23] Owing to these properties, previous studies have explored the use of RuO_2 as an individual coating layer, to enhance the electronic

[a]*Department of Materials Science and Chemical Engineering, Hanyang University, Ansan 15588, Republic of Korea. E-mail: tjp@hanyang.ac.kr*

[b]*Battery Material TU, Samsung Advanced Institute of Technology (SAIT), Samsung Electronics Co., Ltd., Suwon 16678, Republic of Korea*

[c]*Nanocamp Inc., Chungju 27315, Republic of Korea. E-mail: hrkang@nanocamp.kr*

[d]*ALPES Co., Ltd., Ansan 15588, Republic of Korea*

conductivity of CAMs, or additive layer combined with carbon coatings.[24,25] However, for CA-free sintered cathodes, these approaches are intrinsically insufficient to meet the combined requirements of interfacial stabilization and simultaneous Li^+/electron transport. Metallic Ru, while offering high electronic conductivity, lacks Li^+ transport pathways and therefore cannot function as a standalone protective layer. Conversely, RuO_2 enables Li^+ conduction but exhibits lower electronic conductivity than Ru, while carbon-composite strategies inevitably reintroduce inactive components and additional interfacial instability.

In this study, we aim to enhance the electronic conductivity of HTS-LCO while maintaining the Li^+ conduction pathways and suppressing interfacial side reactions. To achieve this, a Ru–RuO_x mixed protective layer (RRML) is deposited on the HTS-LCO surface using ALD without any post-treatment and is applied as an MIEC protective layer. Physicochemical analyses are used to confirm the successful formation of the Ru–RuO_x solid solution, and a full-cell evaluation further demonstrates its impact on electrochemical performance.

Results and discussion

Fig. 1a presents a schematic of the HTS-LCO structure coated with the RRML. Owing to the high step coverage inherent to the ALD process, the three-dimensional surface of LCO can be conformally coated. Fig. 1b and c show the scanning electron microscopy (SEM) images and the corresponding energy-dispersive X-ray spectroscopy (EDS) mapping results for HTS-LCO coated with a 5 nm-thick RRML. The top-view SEM image (Fig. 1b) reveals vertically aligned channels arranged with an interval of approximately 100 μm. In the cross-sectional SEM image (Fig. 1c), the vertical channels extend to a depth of approximately 60 μm, with upper and lower diameters of 40 and 20 μm, respectively. In addition, strong Ru signals are observed across both the HTS-LCO surface and inner region of the channels in the EDS mapping images, indicating the uniform step coverage of the RRML. Fig. 1d and e show the X-ray photoelectron spectroscopy (XPS) results of HTS-LCO coated with a 5 nm-thick RRML. Ar-plasma etching was conducted for 40 s to analyze the chemical-bonding states within the film. Deconvolution of the Ru 3d and C 1s core-level spectra (Fig. 1d) reveals a metallic Ru peak at a binding energy (BE) of ≈280 eV and Ru–O peak at a BE of 280.9 eV. The integrated-area ratio of Ru to RuO_x is approximately 1.5 : 1, indicating that the RuO_x phase constitutes a substantial portion of the film and is consistently present throughout the RRML thickness (Fig. S1). This can be attributed to the island-growth behavior of metallic Ru during the early stages of film deposition, which originates

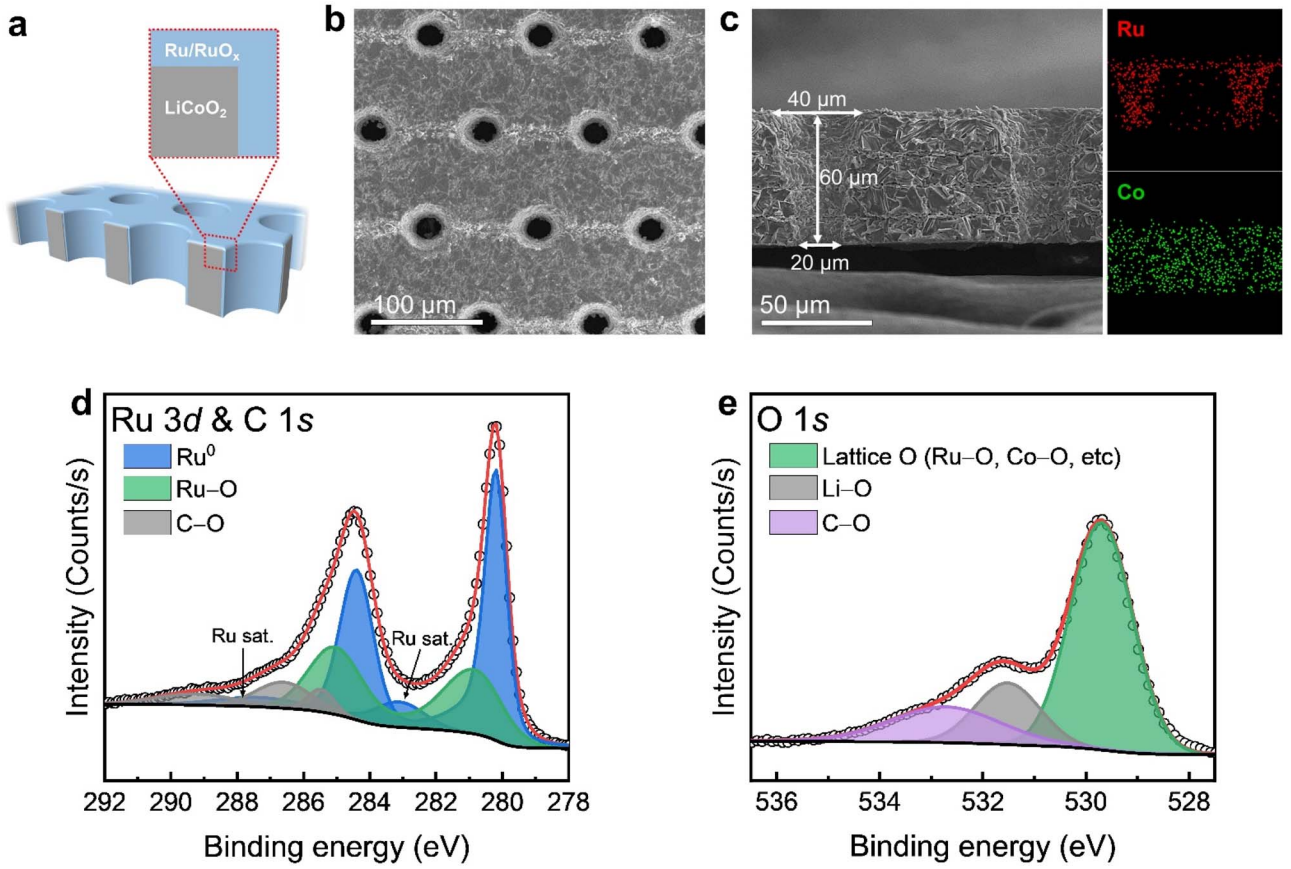

Fig. 1 (a) Schematic of the RRML coated on HTS-LCO *via* ALD, showing conformal coverage on the three-dimensional structured surface. (b and c) Top-view and cross-sectional SEM images and corresponding EDS elemental maps of HTS-LCO with a 5 nm-thick RRML. (d) Ru 3d and C 1s core-level spectra and (e) O 1s core-level spectra of RRML-coated HTS-LCO after 40s etching, indicating the coexistence of metallic Ru and Ru–O bonding in the mixed phase.

from its high surface energy. It is reported that Ru is hardly oxidized when the grain size is below a critical value (<6 nm), due to the increasing oxide formation energy with decreasing grain (island) size.[26,27] Because the film thickness is approximately 5 nm, the grains are extremely small, thereby suppressing oxidation of Ru islands and increasing the relative fraction of thermodynamically unstable grain boundary regions. Oxygen reactants exposed during the ALD process are likely to adsorb at these boundaries. Adsorbed oxygen forms a Ru–O bond at the surface of Ru islands, leading to the formation of the Ru–RuO_x solid solution.[21,28] The O 1s core-level spectra (Fig. 1e) also exhibit a metal–O peak, including Ru–O, at a BE of 529.7 eV, corroborating the interpretation from the Ru 3d spectra and confirming the formation of the RRML on the HTS-LCO surface. In addition, the Co 2p and Li 1s with Co 3p core-level spectra display peaks corresponding to the underlying HTS-LCO (Fig. S2). To assess the MIEC character, the electronic resistivity and ionic conductivity of the RRML were measured (Fig. S3 and Table S1). The film exhibits a low electronic resistivity of $\approx 70\ \mu\Omega\cdot cm^{-1}$ at a thickness of 5 nm and an ionic conductivity of 3.8×10^{-8} S cm^{-1} at 25 °C. These values indicate that the RRML provides simultaneous electronic and ionic transport.

Fig. 2a and b show a cross-sectional high-resolution transmission electron microscopy (HRTEM) image and the corresponding EDS mapping image of HTS-LCO coated with an RRML, respectively. In Fig. 2a, a continuous protective layer is observed, and a strong Ru signal is detected along the HTS-LCO surface in the EDS mapping. This confirms the uniform deposition of the RRML, which is consistent with the SEM–EDS mapping results shown in Fig. 1c. In Fig. 2b, the thickness of the RRML is measured to be approximately 5.5 nm. The fast Fourier transform (FFT) pattern obtained from the HTS-LCO region (lower-right inset in Fig. 2b) displays a distinct diffraction pattern corresponding to the (003) plane of LCO, indicating that negligible structural changes occur in HTS-LCO during the RRML-deposition process. Fig. 2c and d present FFT patterns acquired from local regions within the RRML, in which diffraction spots corresponding to the Ru (101) and (002) planes are observed. Combined with the XPS results shown in Fig. 1d, these observations confirm the presence of a metallic Ru phase within the RRML. Fig. 2e and f show the X-ray diffraction (XRD) results of HTS-LCO coated with 5 and 40 nm-thick RRMLs. Regardless of the RRML thickness, the main diffraction peaks of HTS-LCO at 18.8° and 45.2°, corresponding to the (003) and (104) planes, respectively, remain nearly unchanged,

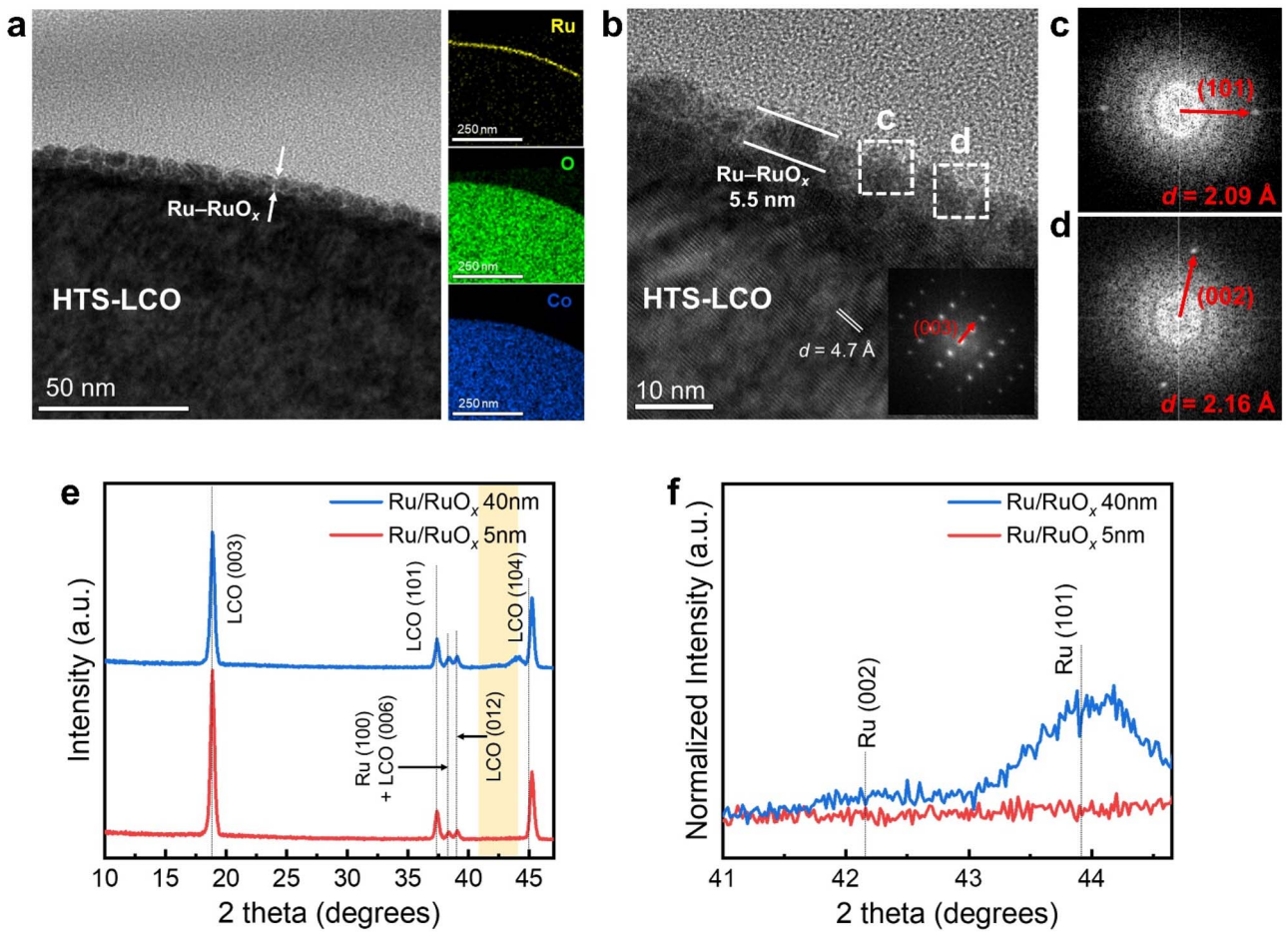

Fig. 2 (a and b) Cross-sectional HRTEM image and corresponding EDS elemental map of HTS-LCO coated with a 5 nm-thick RRML. The inset in (b) shows the FFT pattern corresponding to the (003) plane of LCO. (c and d) FFT patterns obtained from the RRML region, corresponding to the Ru (101) and (002) planes. (e and f) XRD patterns of HTS-LCO with 5 and 40 nm-thick RRMLs.

corroborating the TEM analysis (Fig. 2b) that the ALD process hardly affects the crystal structure of HTS-LCO. However, as shown by the magnified XRD patterns over the 38°–44.6° range (Fig. 2f), a clear difference is observed based on the RRML thickness. For the 5 nm RRML, no apparent diffraction peaks are observed in this region, whereas the 40 nm RRML exhibits the Ru (002) and (101) diffraction peaks at approximately 42.2° and 43.9°, respectively. These results indicate that the absence of diffraction peaks at 5 nm originates from the extremely small grain size of the layer, which is consistent with the previously discussed growth mechanism.

To evaluate the effect of the RRML, full coin-type cells are assembled using uncoated HTS-LCO (bare cell) and RRML-coated HTS-LCO (RRML cell) as the cathodes and graphite as the anode. As shown in Fig. 3a, the bare cell exhibits unstable cycling behavior after approximately 120 cycles and delivers a discharge capacity of 113.9 mAh g^{-1} with 79.3% capacity retention in the 280th cycle. In contrast, the RRML cell retains stable operation for up to 500 cycles and exhibits a capacity retention of 77.6%. The cycle life, defined at 80% capacity retention, is prolonged from 211 to 440 cycles by the RRML coating, reflecting a nearly two-fold enhancement. The rate capability is evaluated by inserting discharge steps at 0.2 and

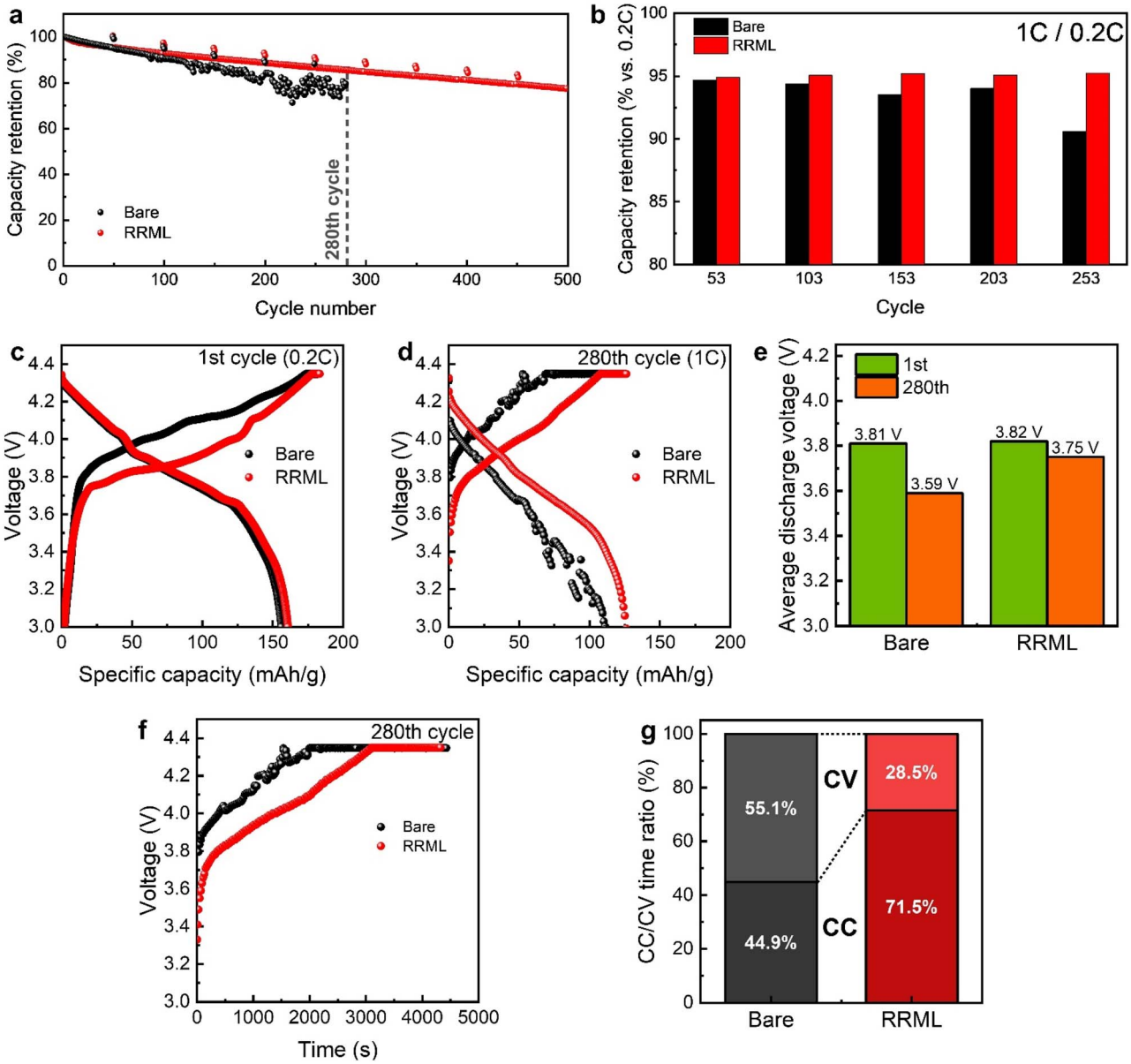

Fig. 3 (a) Cycle performance of full coin-type cells using uncoated HTS-LCO (bare cell) and RRML-coated HTS-LCO (RRML cell) cathodes at 1C. (b) Capacity retention at 1C relative to 0.2C every 50 cycles, showing suppressed resistance growth for the RRML cell. (c and d) Charge–discharge profiles of the bare and RRML cells in the 1st cycle (0.2C) and 280th cycle (1C). (e) Average discharge voltages in the 1st and 280th cycles. (f) Voltage–time profiles and (g) CC/CV time ratios in the 280th cycle, showing longer CC duration and reduced interfacial polarization for the RRML-coated cell.

0.5C every 50 cycles (Fig. 3b). The bare cell exhibits a 1C capacity retention of 94.7% relative to 0.2C in the 53rd cycle, which decreases to 90.6% in the 253rd cycle. In contrast, the RRML cell exhibits nearly constant capacity retentions between 94.9% and 95.2% under identical conditions. These results suggest that the bare cell becomes increasingly limited by nonuniform charge transfer and localized polarization associated with the absence of a CA, accompanied by progressive interfacial processes that are consistent with an increase in interfacial resistance during cycling.[29–32]

Fig. 3c presents the charge–discharge profiles of the bare and RRML cells in the first cycle (0.2C), and Fig. 3d shows those in the 280th cycle (1C). The corresponding average discharge voltages are shown in Fig. 3e. At the beginning of the 1C discharge in the 280th cycle (Fig. 3d), the bare cell exhibits a voltage decrease of 0.253 V, whereas the RRML cell exhibits a decrease of only 0.096 V. The average discharge voltages of the bare and RRML cells are 3.81 and 3.86 V in the first cycle (0.2C) and 3.59 and 3.75 V in the 280th cycle (1C), respectively. Consequently, the decreases in the average discharge voltage from the first to the 280th cycle are 0.22 and 0.076 V for the bare and RRML-coated cells, respectively, representing a nearly threefold difference. These results are consistent with reduced interfacial impedance growth in the RRML cell under high-rate operation, supporting its role in stabilizing charge-transfer behavior at the cathode–electrolyte interface. Fig. 3f presents the voltage–time profile of the cells in the 280th cycle, while Fig. 3g summarizes the relative durations of the constant-current (CC) and constant-voltage (CV) charging steps. In general, a reduced CC-time ratio indicates that the cell reaches the cut-off voltage prematurely owing to increased polarization, which is primarily associated with elevated interfacial resistance at the cathode–electrolyte interface.[33,34] Under such conditions, the CC step terminates earlier, and a prolonged CV step follows. In the 280th cycle, the CC charging times of the bare and RRML cells are 1991 and 3093 s, corresponding to CC-time ratios of 44.9% and 71.5%, respectively, representing a 1.6-fold difference. The markedly shorter CC step of the bare cell reflects severe interfacial polarization, whereas the extended CC step of the RRML cell indicates suppressed polarization buildup during charging. This interpretation is further supported by electrochemical impedance spectroscopy (EIS) performed after the formation cycles, where the RRML cell exhibits a lower charge-transfer resistance ($R_{ct} \approx 36.8\ \Omega$) than the bare cell ($R_{ct} \approx 51.9\ \Omega$), indicating reduced interfacial impedance at the cathode–electrolyte interface (Fig. S4 and Table S2). Taken together, the polarization behavior, CC/CV time-ratio evolution, and EIS results consistently indicate mitigated interfacial-impedance buildup in the RRML cell during long-term cycling.

Conclusions

In this study, an Ru–RuO_x mixed protective layer (RRML) was deposited on the surface of high-density three-dimensional sintered LCO (HTS-LCO) *via* ALD to improve electronic and ionic conduction while mitigating interfacial side reactions. XPS analysis of the 5 nm-thick film confirmed the formation of a Ru–RuO_x solid solution, where Ru-related diffraction peaks were not clearly detected in XRD owing to the extremely small grain size. These results demonstrate that the initial island-growth behavior of Ru enabled the deposition of a RRML without post treatment. The full-cell evaluation revealed that the RRML coating improved the cycling performance of HTS-LCO. Under high-rate (1C) conditions, the RRML-coated cell reached 80% capacity retention in the 440th cycle, whereas the uncoated HTS-LCO cell reached the same level in the 211th cycle, corresponding to a two-fold enhancement in cycle life. Furthermore, the decreases in the average discharge voltage between the first (0.2C) and 280th (1C) cycles were 0.076 and 0.22 V for the RRML-coated and uncoated cells, respectively, representing a threefold difference. Moreover, the CC-time ratio exhibited a 1.6-fold increase. These findings experimentally confirmed that the RRML simultaneously provided efficient Li^+ and e^- conduction pathways as a MIEC protective layer, thereby offering a practical route toward the design of CA-free high-density electrodes.

Experimental

Film preparation

ALD of the RRML was conducted on a 6-inch-diameter scale, traveling-wave-type reactor (ALPES Co., Ltd.) at 265 °C. (Ethylbenzene)(1-ethyl-1,4-cyclohexadiene) ruthenium(0) (EBE-CHRu, Hansol Chemical) was used as the precursor, and it was heated to 100 °C. High-purity N_2 (99.999%) was used as the purge/carrier gas at a flow rate of 100 sccm. High-purity O_2 (99.999%) was used as the reactant at a flow rate of 100 sccm. The ALD process used for the RRML consisted of 4 s (Ru precursor)–30 s (N_2 purge)–15 s (O_2)–30 s (N_2 purge) (Fig. S5). 5 nm-and 40 nm-thick RRMLs were grown using 40 and 320 ALD cycles, respectively.

Material characterization

The chemical states of RRMLs were analyzed using XPS (K-Alpha, Thermo Fisher Scientific Co). Field-emission SEM (FE-SEM; S-4800, Hitachi) was used to analyze the structure of HTS-LCO and uniformity of the film. The thicknesses and morphologies of the RRMLs were examined using a 200 kV field-emission TEM (JEM-2100F, JEOL). The TEM specimens were prepared using focused ion-beam etching (Quanta 3D FEG, FEI). The crystal structures of the HTS-LCO and RRMLs were confirmed using XRD (Smartlab, Rigaku).

Electrochemical characterization

The cathode (HTS-LCO) and anode (graphite) were prepared following the procedure reported by Kim *et al.*[7] The cells were assembled using these electrodes, a 14 μm-thick polyethylene separator coated with a ceramic layer, and an electrolyte composed of 1.15 M $LiPF_6$ dissolved in ethylene carbonate, ethyl methyl carbonate, and dimethyl carbonate with a volume ratio of 3 : 4 : 3. Moreover, 2032-type coin cells were assembled in an Ar-filled glove box. After 24 h rest at 25 °C, the cells were tested with a battery-cycle tester (TOSCAT, Toyo). Charge–discharge

tests were conducted within a voltage window of 3.0–4.35 V. The cells were charged to 4.35 V at 0.1C in CC mode, followed by CV charging at 4.35 V until the current decreased to 0.05C. The discharge process was performed at 0.1C to 3.0 V in CC mode. Three formation cycles were carried out under these conditions, followed by cycling at 0.2C (1 cycle), 0.5C (1 cycle), and 1C (48 cycles) within the same voltage range. All electrochemical measurements were conducted at 25 °C.

Author contributions

Kyu Moon Kwon: writing – original draft, validation, formal analysis, investigation, methodology, data curation, visualization. Ji Won Han: formal analysis, investigation, methodology, data curation. Joungwon Park: formal analysis, investigation, resources, data curation. Kyoung Hwan Kim: investigation, resources. Hwi-Yeol Park: resources, supervision. Woo-Hee Kim: supervision. Ji-Hoon Ahn: supervision. Hyo Rang Kang: writing – review & editing, conceptualization, supervision. Tae Joo Park: writing – review & editing, conceptualization, supervision, project administration, funding acquisition. All authors have given approval to the final version of the manuscript.

Conflicts of interest

There are no conflicts to declare.

Data availability

The data that support the findings of this study are available from the corresponding author upon reasonable request.

Supplementary information (SI) is available. See DOI: https://doi.org/10.1039/d5ta09872f.

Acknowledgements

This work was supported by the Samsung Advanced Institute of Technology (April 2020–April 2021). This work was supported by K–CHIPS (Korea Collaborative & High-tech Initiative for Prospective Semiconductor) Research (2410012361, RS-2025-02305609, and 25067-15FC) funded by the Ministry of Trade, Industry & Energy (MOTIE, Korea).

References

1 Y. Huang, M. Zhu, Y. Huang, Z. Pei, H. Li, Z. Wang, Q. Xue and C. Zhi, *Adv. Mater.*, 2016, **28**, 8344–8364.
2 Q. Xue, J. Sun, Y. Huang, M. Zhu, Z. Pei, H. Li, Y. Wang, N. Li, H. Zhang and C. Zhi, *Small*, 2017, **13**, 1701827.
3 H. Zheng, R. Yang, G. Liu, X. Song and V. S. Battaglia, *J. Phys. Chem. C*, 2012, **116**, 4875–4882.
4 W. Lai, C. K. Erdonmez, T. F. Marinis, C. K. Bjune, N. J. Dudney, F. Xu, R. Wartena and Y.-M. Chiang, *Adv. Mater.*, 2010, **22**, E139–E144.
5 K. G. Gallagher, S. E. Trask, C. Bauer, T. Woehrle, S. F. Lux, M. Tschech, P. Lamp, B. J. Polzin, S. Ha, B. Long, Q. Wu, W. Lu, D. W. Dees and A. N. Jansen, *J. Electrochem. Soc.*, 2016, **163**, A138.
6 H. Jeong, S.-J. Lim, S. Chakravarthy, K. H. Kim, J. Lee, J. S. Heo and H. Park, *J. Power Sources*, 2020, **451**, 227764.
7 K. H. Kim, H. Jeong, H. C. Lee, J. K. Shon, J. Park and H.-Y. Park, *J. Power Sources*, 2022, **551**, 232223.
8 K. Edström, T. Gustafsson and J. O. Thomas, *Electrochim. Acta*, 2004, **50**, 397–403.
9 M. Gauthier, P. Karayaylali, L. Giordano, S. Feng, S. F. Lux, F. Maglia, P. Lamp and Y. Shao-Horn, *J. Electrochem. Soc.*, 2018, **165**, A1377.
10 J.-N. Zhang, Q. Li, Y. Wang, J. Zheng, X. Yu and H. Li, *Energy Storage Mater.*, 2018, **14**, 1–7.
11 C. Li, H. P. Zhang, L. J. Fu, H. Liu, Y. P. Wu, E. Rahm, R. Holze and H. Q. Wu, *Electrochim. Acta*, 2006, **51**, 3872–3883.
12 S. Kalluri, M. Yoon, M. Jo, H. K. Liu, S. X. Dou, J. Cho and Z. Guo, *Adv. Mater.*, 2017, **29**, 1605807.
13 Z. Chen, Y. Qin, K. Amine and Y. K. Sun, *J. Mater. Chem.*, 2010, **20**, 7606–7612.
14 D. Weber, Đ. Tripković, K. Kretschmer, M. Bianchini and T. Brezesinski, *Eur. J. Inorg. Chem.*, 2020, **2020**, 3117–3130.
15 S. M. George, A. W. Ott and J. W. Klaus, *J. Phys. Chem.*, 1996, **100**, 13121–13131.
16 S. M. George, *Chem. Rev.*, 2010, **110**, 111–131.
17 M. Lee, W. Ahmad, D. W. Kim, K. M. Kwon, H. Y. Kwon, H.-B. Jang, S.-W. Noh, D.-H. Kim, S. J. A. Zaidi, H. Park, H. C. Lee, M. Abdul Basit and T. J. Park, *Chem. Mater.*, 2022, **34**, 3539–3587.
18 C. M. Hayner, X. Zhao and H. H. Kung, *Annu. Rev. Chem. Biomol. Eng.*, 2012, **3**, 445–471.
19 S. P. Culver, R. Koerver, W. G. Zeier and J. Janek, *Adv. Energy Mater.*, 2019, **9**, 1900626.
20 D. Gall, *J. Appl. Phys.*, 2016, **119**, 085101.
21 J. W. Han, H. S. Jin, Y. J. Kim, J. S. Heo, W.-H. Kim, J.-H. Ahn, J. H. Kim and T. J. Park, *Nano Lett.*, 2022, **22**, 4589–4595.
22 P. Balaya, H. Li, L. Kienle and J. Maier, *Adv. Funct. Mater.*, 2003, **13**, 621–625.
23 O. Delmer and J. Maier, *Phys. Chem. Chem. Phys.*, 2009, **11**, 6424–6429.
24 R. Zhang, Y. Zhang, K. Zhu, F. Du, Q. Fu, X. Yang, Y. Wang, X. Bie, G. Chen and Y. Wei, *ACS Appl. Mater. Interfaces*, 2014, **6**, 12523–12530.
25 S. H. Jung, D. H. Kim, P. Brüner, H. Lee, H. J. Hah, S. K. Kim and Y. S. Jung, *Electrochim. Acta*, 2017, **232**, 236–243.
26 G. M. Dalpain and J. R. Chelikowsky, *Phys. Rev. Lett.*, 2006, **96**, 226802.
27 R. Methaapanon, S. M. Geyer, S. Brennan and S. F. Bent, *Chem. Mater.*, 2013, **25**, 3458–3463.
28 M. G. Kozodaev, Y. Y. Lebedinskii, A. G. Chernikova, E. V. Korostylev, A. A. Chouprik, R. R. Khakimov, A. M. Markeev and C. S. Hwang, *J. Chem. Phys.*, 2019, **151**, 204701.
29 J. Entwistle, R. Ge, K. Pardikar, R. Smith and D. Cumming, *Renew. Sustain. Energy Rev.*, 2022, **166**, 112624.
30 L. Wen, L. Wang, Z. Guan, X. Liu, M. Wei, D. Jiang and S. Zhang, *Ionics*, 2022, **28**, 3145–3153.

31 M. D. Bouguern, A. K. M R and K. Zaghib, *J. Power Sources*, 2024, **623**, 235457.
32 A. S. Mussa, A. J. Smith, G. M. Trippetta, G. Lindbergh, M. Klett and R. W. Lindström, *J. Energy Storage*, 2025, **114**, 115869.
33 T. Bartsch, A. Y. Kim, F. Strauss, L. de Biasi, J. H. Teo, J. Janek, P. Hartmann and T. Brezesinski, *Chem. Commun.*, 2019, **55**, 11223–11226.
34 V. J. Ovejas and A. Cuadras, *J. Power Sources*, 2019, **418**, 176–185.